ACS OMEGA

Open Access

http://pubs.acs.org/journal/acsodf

Article

Transforming Natural Eggshell and Diatomite into Bioactive Calcium Silicate Material for Bone Regeneration

Haiming Yu,[§] Zhihua Liu,[§] Lingying Chen, Xiaoyu He, Yiyong Weng, Weizhe Li, Xiaozhi Zheng, Qunlong Pan, Rongmou Zhang, Xiaoyan Zhang, and Wenhua Wu*

Cite This: *ACS Omega* 2024, 9, 19440−19450

Read Online

ACCESS | Metrics & More | Article Recommendations

ABSTRACT: Calcium silicate (CS), a new and important bioceramic bone graft material, is prepared by using eggshells, which have a porous structure and are rich in calcium ions. Furthermore, the preparation of new CS materials using eggshells and diatomaceous earth minimizes their negative impact on the environment. In this study, we prepared CS materials using a high-temperature calcination method. The composition of the material was demonstrated by X-ray diffraction (XRD) and Fourier transform infrared spectroscopy (FTIR) analysis. Scanning electron microscopy (SEM) analysis confirmed the porous structure of the CS material. We also introduced ZnO to prepare ZnO−CS with antibacterial properties and showed that ZnO−CS exhibits excellent antibacterial effects through *in vitro* antibacterial experiments. Subsequent *in vitro* mineralization experiments demonstrated that ZnO−CS promoted the formation of a hydroxyapatite layer. Furthermore, *in vitro* cytotoxicity experiments demonstrated that ZnO−CS had very good biosafety and promoted cell proliferation. These findings were confirmed through subsequent cell proliferation experiments. Our results indicate that the novel ZnO−CS is a promising candidate for bone tissue engineering.

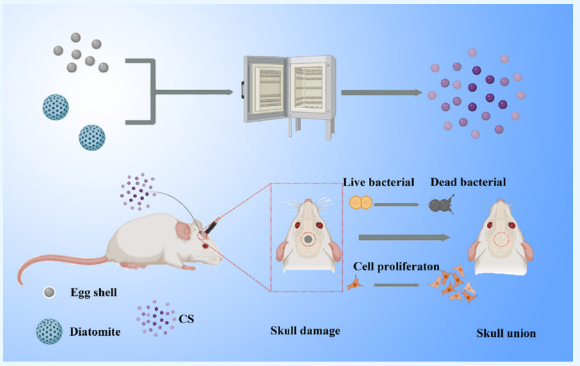

1. INTRODUCTION

Bone defects have various clinical causes including infection, trauma, and cancer.[1] Over 2.2 million bone graft procedures are performed every year globally to repair bone defects during neurological, oral and maxillofacial, and orthopedic surgeries.[2] While autologous bone grafts are the gold standard for bone repair,[3] their use is limited due to the scarcity of suitable sources and high rate of complications in the bone extraction area, such as infection, pain, and hematoma.[4,5] Although allogeneic bone grafts of animal origin are abundant, they are prone to immune rejection and carry a potential risk of disease transmission.[6] As a result, new bone graft replacement materials offering good biocompatibility and osteoinductivity are of great interest.

Traditional biological replacement materials mainly come under the following three categories: bioinert materials, bioactive materials, and bioactive materials with bone induction.[7] Among them, bioinert materials do not cause immune rejection, but instead play a partial supporting role and are gradually eliminated.[8] Bioactive materials can trigger certain biological reactions at the interface, but they do not have effective osteogenic effect, and the osteogenic effect is not good.[9] Bioceramic materials with bone-inducing effects are typically composed of calcium phosphate, calcium sulfate, and hydroxyapatite (HA). They have been shown to have good histocompatibility and bioactivity.[10] However, these materials have limitations such as insufficient osteogenic induction, low mechanical strength, a repair rate mismatch with bone tissue, and insufficient antibacterial properties.[11,12] Calcium silicate-based biomaterials have demonstrated improved efficacy effective in promoting bone marrow mesenchymal stem cell proliferation, osteogenic differentiation, and bone formation than conventional calcium−phosphorus-based materials.[1,13] The presence of Ca in calcium silicate (CS) can help promote the production of the calcium−phosphorus layer and the growth of new bone.[14] However, most CS is synthesized from industrial materials, resulting in significant pollution; furthermore, the raw materials are limited and nonbiodegradable.[15−17] Therefore, the use of biological materials, such as eggshells and diatomaceous earth, may be beneficial for CS synthesis.

A large amount of eggshells is discarded daily as waste, leading to significant pollution. Organic substances and

Received: January 28, 2024
Revised: March 2, 2024
Accepted: April 5, 2024
Published: April 18, 2024

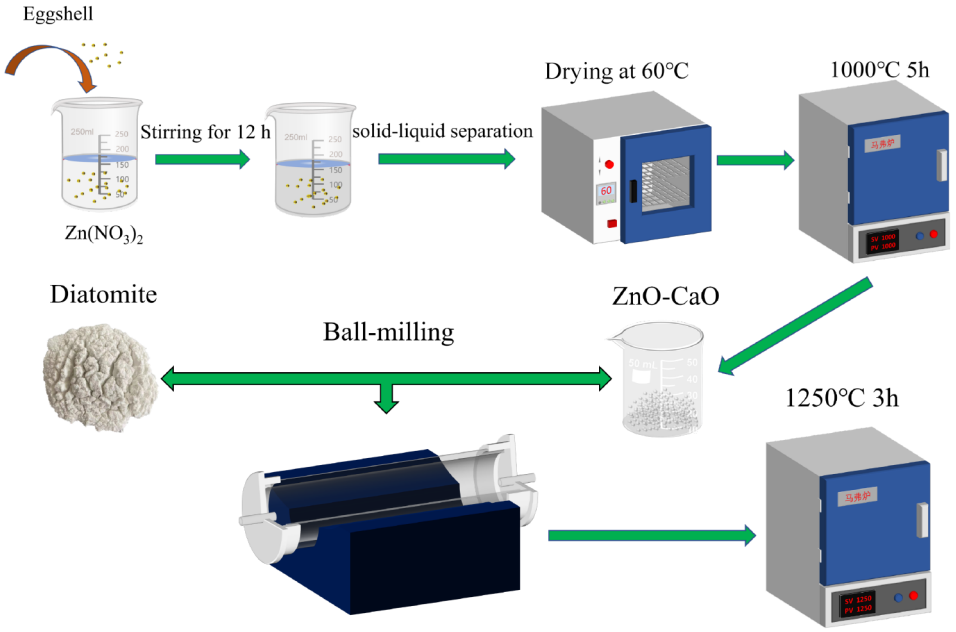

Figure 1. Flowchart of the preparation of ZnO−CS.

minerals in eggshells may enter water bodies during degradation and cause water pollution. In addition, the carbon dioxide and hydrogen sulfide released by their degradation will lead to an increase in the concentration of harmful gases in the air, causing air pollution.[18] However, the high biological activity of eggshells makes them potentially useful for biological and pharmaceutical applications.[19−22] Natural eggshells are hierarchically assembled porous composite materials composed of $CaCO_3$ minerals and biomolecules. The Ca^{2+} ions and carbonates released by eggshells provide a suitable microenvironment for new bone regeneration.[23] Furthermore, trace elements such as Mg, P, Sr, and Na in eggshells play important roles in promoting angiogenesis and osteogenesis.[21,24] Both eggshells and diatomaceous earth inherently have porous structures.[25] The porous structure of these materials facilitates not only their degradation but also the growth and metabolism of new tissues.[26,27]

One of the complications of bone graft surgery is infection, which can lead to the resorption of bone grafts and failure of bone fusion. Therefore, the ideal bone cement should have the ability to promote the osteogenic activity of osteoblasts while inhibiting bacterial growth.[28,29] Antimicrobial drugs can help address the challenges posed by drug-resistant bacterial infections.[30] ZnO is an antimicrobial material that has been widely used and demonstrated excellent antibacterial effects.[31−34] Felice et al.[35] prepared a polycaprolactone/ZnO/HA scaffold and found that after doping with ZnO, the scaffold exhibited good antibacterial activity and promoted early cell mineralization induction by the scaffold at a high concentration of ZnO.

This study aimed to create a new environmentally friendly and cost-effective CS material from household waste eggshells and diatomaceous earth supplemented with ZnO. We hypothesized that the novel CS material would promote bone regeneration and have antibacterial properties, with the potential to be adopted as a bioceramic option in the field of bone transplantation.

2. MATERIALS AND EXPERIMENTAL

2.1. Materials. The eggshells used in this study were acquired from the canteen at the Quanzhou Normal University. Analysis pure grade diatomite (AR.500 g) was purchased from Fuchen Chemical Reagents Ltd. Zinc nitrate hexahydrate ($Zn(NO_3)_2{\cdot}6H_2O$) was obtained from Sinopharm Chemical Reagent Company. Nutrient Agar and Nutrient Broth were purchased from Shanghai Bowei Biotechnology Company, and bacteria were obtained from the Second Affiliated Hospital of Fujian Medical University. MG-63 cells were purchased from Wuhan Procell Life Science and Technology Co., Ltd. Dulbecco's modified eagle medium (DMEM) and penicillin-streptomycin medium were obtained from Thermo Fisher Scientific Co., Ltd. Special fetal bovine serum and Cell Counting Kit-8 (CCK-8) reagent were acquired from Hefei Clark Bioscience Co. Calcein/PI Cell Activity and Cytotoxicity Assay Kit was purchased from BiyunTian Ltd.

2.2. Preparation of ZnO-$CaSiO_3$. The eggshells were soaked in deionized water for 2 h, following which the shell membranes were removed. The eggshells were repeatedly cleaned and dried in a vacuum drying oven at 60 °C for 6 h. Next, the eggshells were ground in an agate mortar and passed through a 200-mesh sieve for later use. To prepare the ZnO-CaO, 50 g of eggshell powder was added to 500 mL of 0.02 M $Zn(NO_3)_2$ and soaked for 12 h with constant stirring. The mixture was separated by solid/liquid, and the supernatant was discarded. The precipitate was dried in an oven at 60 °C and then was removed. To obtain ZnO-CaO, 50 g of the precipitate was placed in a Muffle furnace (Hefei Kojing Material Technology Co., Ltd.) at 1000 °C for 5 h, followed by cooling to room temperature. Subsequently, 20g of ZnO-CaO and 10.7 g of diatomite were mixed in a planetary ball mill for 6 h at a molar ratio of 1:1. The mixture was then poured into a porcelain boat and then calcined in a Muffle furnace at 1250 °C for 3 h to obtain ZnO-$CaSiO_3$ (ZnO−CS). The chemical reaction equation for this process is $SiO_2 + CaO = CaSiO_3$

https://doi.org/10.1021/acsomega.4c00904
ACS Omega 2024, 9, 19440−19450

(conditions are at a high temperature). The reaction flowchart is shown in Figure 1.

2.3. Characterizations. The crystalline structure of ZnO−CS was evaluated using X-ray diffraction (XRD, Bruker D8 Advance, Germany) analysis in the 2θ range of 5−80° with a step scan of 1.8°/min. The chemical bonds and functional groups of ZnO−CS were analyzed using Fourier transform infrared spectroscopy (FTIR Thermo Scientific, USA) in the range 4000−500 cm^{-1}. Brunauer−Emmett−Teller (BET) surface areas were calculated at 77 K by using the JWGB instrument (JW-DEL 200). To prepare the studied nanopowders, an overnight degassing phase was applied under high vacuum conditions, and liquid nitrogen was used to cool the samples. After degassing, N_2 gas was injected to adsorb in the samples, and desorption was performed at a specific pressure. Parameters such as the BET-specific surface area were calculated based on the adsorption−desorption curve at P/P_0 = 0.995, assuming complete pore saturation. The surface electronic state and elemental composition of the CS nanocomposite nanomaterials were analyzed by X-ray photoelectron spectroscopy (XPS). The C peak was corrected by using the C1S peak at 284.8 eV and then corrected for other peaks. The morphologies of eggshell meal, diatomite, and ZnO−CS morphology were observed using a scanning electron microscope (SEM, Zeiss, Germany) after sputter coating with a thin layer of platinum (20 mA, 120 s).

2.4. *In Vitro* Degradation Test. The degradation rate of the ZnO−CS materials was evaluated by immersing them in simulated body fluid (SBF) solutions where the ion concentrations are summarized in Table 1, at a volume ratio of 200 mL/g at 37 °C. The SBF solution was prepared using the method proposed by Kobubo.[36] The weight loss of the ZnO−CS material and the pH values of the medium were recorded at predetermined time intervals of 1, 3, 5, 7, and 14 days. The degradation rate was calculated using the following formula:

Table 1. SBF Versus Plasma Ion Concentration

ion	ion concentration in plasma (mM)	ion concentration in SBF (mM)
Na^+	142.0	142.0
K^+	5.0	5.0
Mg^{2+}	1.5	1.5
Ca^{2+}	2.5	2.5
Cl^-	103.0	147.8
HCO_3^-	27.0	4.2
HPO_4^-	1.0	1.0
SO_4^{2-}	0.5	0.5
pH	7.2−7.4	7.4

$$\text{Weight loss} = (W_0\text{-}W_i)/W_0 \times 100\%$$

where W_0 is the initial weight and W_i is the weight of the sample after drying.

2.5. *In Vitro* Bioactivity Test. To observe the *in vitro* osteointegration ability of the prepared samples, the formation of a hydroxyapatite (HAp) layer on the surfaces was tested. The sintered ceramic masses were immersed in SBF solution and incubated at 37 °C under static conditions for 1, 3, 5, and 7 days. After each immersion period, the samples were removed from the SBF solution, washed with deionized water, dried at room temperature, and observed for the formation of the apatite layer under electron microscopy.

2.6. Antimicrobial Activity. The antibacterial ability of ZnO−CS nanocomposites against *E. coli* and *S. aureus* was evaluated using an agar diffusion assay. Sterilized agar solution was poured into sterile culture dishes and allowed to solidify. The agar plates were inoculated with *E. coli* and *S. aureus*, respectively, and the prepared ZnO−CS and CS sample wafers were put into the plates with different bacterial solutions. Finally, the Petri dishes were sealed and incubated in a constant temperature incubator at 37 °C for 24 h, after which the size of the inhibition zones on the plates was measured. In addition, the antibacterial effect of ZnO−CS was further tested by a bacterial counting method.

2.7. *In Vitro* Cell Experiment of CS. *2.7.1. Preparation and Culture of Cells.* MG-63 cells were acquired from Procell Life Science and Technology Co., Ltd. Special fetal bovine serum and CCK-8 assay reagent were purchased from Clark Bioscience Co. High glucose DMEM was purchased from Thermo Fisher Scientific Co., Ltd. The Ethics Committee of Fujian Medical University approved the application for *in vitro* study of the cells. MG-63 cells were cultured in DMEM supplemented with 10% fetal bovine serum, 100 U/mL penicillin, and 100 mg/mL streptomycin (Thermo Fisher Scientific Co., Ltd.) and incubated in a CO_2 incubator at 37 °C with 5% CO_2. The medium was refreshed every other day.

2.7.2. In Vitro Cytotoxicity Test. MG-63 cells were inoculated in 96-well plates at a density of 2×10^4/well and incubated in a cell culture incubator for 24 h. Each group was treated with CS for 24 h by adding different concentrations of CS extract, and three replicate wells were set up in a group. Then, 10 μL of CCK-8 solution was added to each well and incubated at 37 °C for 1.5 h. The optical density (OD) was measured at 450 nm using an enzyme marker (Tecan Sunrise, Switzerland). The cellular viability was calculated according to the following equation:

$$\text{Cell viability (\%)} = \frac{A_t\text{-}A_h}{A_c\text{-}A_b} \times 100\%$$

where A_t is the absorption of solutions containing different concentrations of ZnO−CS, A_c is the absorption of the control sample, and A_b is the absorption of cell-free solutions.

In addition, the optimal ZnO−CS concentration was selected to intervene the cells using the material, which was then stained with a live−dead cell stain to assess the cytotoxicity of the material.

2.7.3. Cell Proliferation Assay. The effect of the CS dosage on cell viability was evaluated using the CCK-8 method. Sterilized ZnO−CS was placed in 96-well plates, and 1 mL of cell suspension with a concentration of 1×10^4 cells/mL was added to each well and cultured for 1, 3, and 7 days. After completion of the culture, the medium containing 10% CCK-8 was replaced, and the plates were incubated for 2 h. Finally, 100 μL of the liquid was transferred from the 24-well plate to a 96-well plate, and the OD values were measured at 450 nm by using an enzyme marker.

2.8. *In Vivo* Study. *2.8.1. Animal Preparation and Surgical Phases.* To investigate the efficacy of the new CS material *in vivo* for bone defect repair, 24 male Sprague−Dawley (SD) rats, aged 8 weeks and weighing 250 ± 25 g, were chosen for the experiments. SD rats were selected because their bone structure and physiological mechanisms

https://doi.org/10.1021/acsomega.4c00904
ACS Omega 2024, 9, 19440−19450

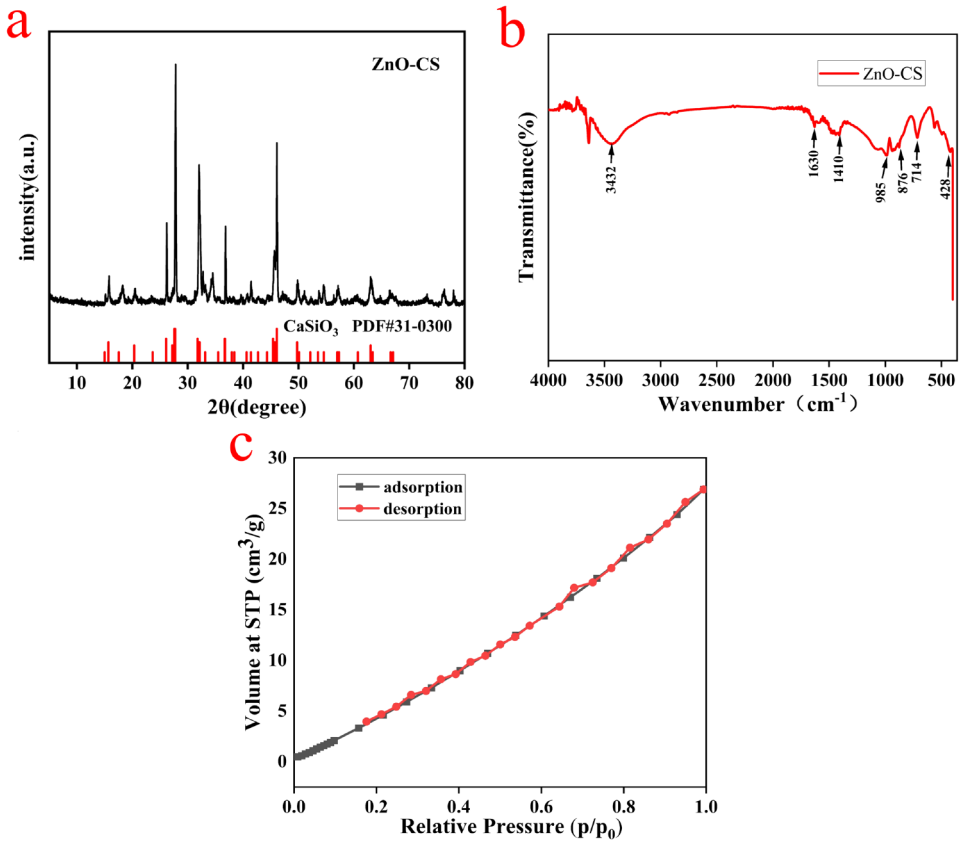

Figure 2. (a) X-ray diffraction pattern of porous ZnO−CS sintered at 1250 °C. (b) FTIR test result of ZnO−CS. (c) Nitrogen adsorption−desorption isotherms on ZnO−CS.

closely resemble those of humans. Specifically, their bone growth and regeneration processes exhibit a high similarity to those observed in humans, making them a suitable model for simulating human bone grafting.

The new CS material was sterilized by using UV light irradiation. A symmetrical defect hole, with a diameter of 5 mm (considered to be the minimum size for verifying bone defect repair),[37] was drilled in the center of each rat's skull using a drill hole. The rats were randomly divided into three groups. One group served as a blank control, with the defect left unfilled to serve as a reference. The remaining two test groups included rats with the defect filled with the new CS material and ZnO−CS. All rats underwent a 24-h fasting period prior to the surgery.

2.8.2. CT Analysis. At 4 and 8 weeks, four rats from each group were sacrificed, and their skulls were dissected to separate the bones from the surrounding muscles and fascia. The specimens were then immersed in a 4% paraformaldehyde solution overnight for fixation. Subsequently, a CT system was employed to scan the samples and evaluate the formation of new bone in the defect area. Following the scanning process, the raw data were imported into GEHC Microview software to generate three-dimensional images. With the assistance of the software, new bone tissue was identified.

2.8.3. Histological Analysis. The fixed tissues were subjected to decalcification using a 25% formic acid decalcification solution for 48 h, followed by rinsing with running water for 24 h. Gradual dehydration was performed using ethanol, and then, the tissues were embedded in paraffin wax and sliced into 4 μm sections. Subsequently, they were rinsed with xylene and different concentrations of ethanol. Finally, the sections were subjected to treatment with hematoxylin and eosin (H and E) and staining with Masson's trichrome. The results of the stained sections were documented using a light microscope.

2.9. Statistical Treatment. All results are expressed as mean ± standard deviation (SD). One-way ANOVA was performed using the statistical software SPSS 10.0 (Chicago, USA). $p < 0.05$ indicates a statistical difference.

3. RESULTS AND DISCUSSION

3.1. Characterization Testing of Materials. *3.1.1. XRD, FT-IR, and BET Analysis.* The XRD pattern of the sample sintered at 1250 °C is shown in Figure 2a. The diffraction peaks of the CS samples appeared at 29.1, 31.0, 32.0, 32.1, 32.6, 32.7, 32.8, 34.1, 41.1, and 45.7, corresponding to (0 0 2), (1 1 1 2), (1 2 0), (−1 0 3), (−1 2 1), (2 0 0), (0 2 2), (1 2 1), (1 0 3), and (−2 2 2), respectively. Almost all of the sample peaks overlapped with the standard peak positions (standard card no. 31−0300) and matched well, indicating that the prepared sample was $CaSiO_3$. The characteristic peak of ZnO was not observed due to the small concentration of eggshell-loaded ZnO.

Figure 2b shows the FTIR spectra of the ZnO−CS samples calcined at 1250 °C. The Q2 tetrahedral Si−O stretching vibration band at ∼985 cm^{-1} and the Q1 tetrahedral Si−O stretching vibration band at 876 cm^{-1} are visible. The peak at 1024 cm^{-1} is attributed to Si−O−Si symmetric tensile vibration.[38] The absorption bands near 985 cm^{-1}, 714 cm^{-1}, and 428 cm^{-1} are characteristic absorption bands of high-

https://doi.org/10.1021/acsomega.4c00904
ACS Omega 2024, 9, 19440−19450

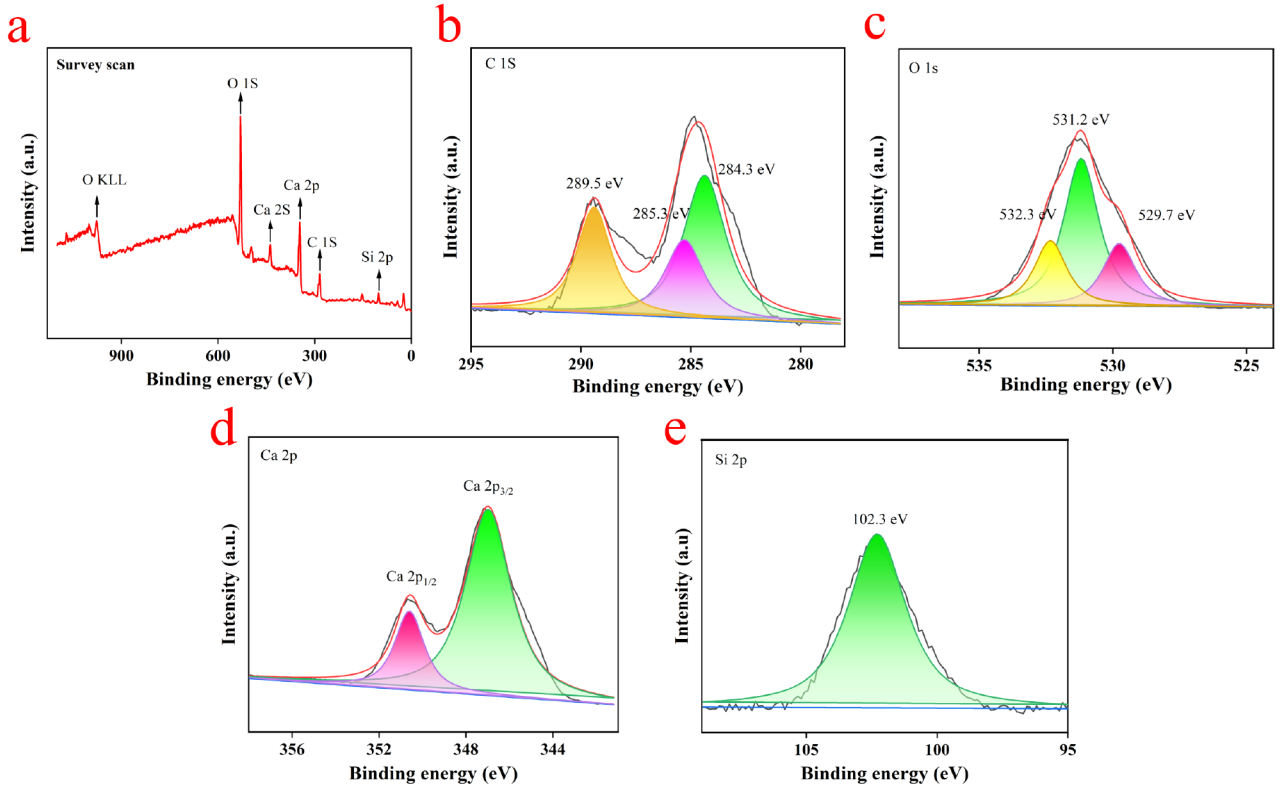

Figure 3. XPS spectra of CS composite: (a) full spectra; (b) C 1S; (c) O 1S; (d) Ca 2p and (e) Si 2p spectra.

temperature type wollastonite with a ternary ring structure.[39] The asymmetric stretching of 1410 cm^{-1} is due to the dissolution of CO_2 in silicate bioceramics, which leads to the formation of distorted carbonate groups where the CO_2 absorbed during the reaction may be of environmental origin. The bending vibration of H_2O is observed at 1630 cm^{-1}, and a broad moisture absorption band was observed at 3432 cm^{-1}.[40]

The adsorption−desorption isotherm of nitrogen (Figure 2c) was used to calculate the average BET-specific surface area of ZnO−CS, which was found to be 23.61 m^2/g. The total adsorption pore volume was 0.072 cm^3/g.

3.1.2. XPS Analysis. To characterize the surface electronic state and elemental composition of CS composite nanomaterials, XPS analysis was performed.

Figure 3 displays the full-scan spectrum of the CS nanocomposite, revealing the presence of four elements: C, O, Ca, and Si, thereby confirming the high purity of the prepared CS. In Figure 3, the C 1S spectrum of CS shows three peaks at 284.3, 285.3, and 289.5 eV, corresponding to C−C, C−O−C, and O—C═O bonds, respectively.[41] The lack of elemental C in the sample and the presence of the C peak may suggest potential airborne C contamination. The O1S spectrum was analyzed (Figure 3c), indicating C=O (529.7 eV), C−O (531.2 eV), and O−H (532.3 eV) bonding states.[42] An additional auger peak of O was observed at 977.2 eV. The Ca 2p XPS spectrum is depicted in Figure 3, with peaks centered at 346.8 and 350.5 eV, separated by 3.7 eV, which can be attributed to the Ca $2p_{3/2}$ and Ca $2p_{1/2}$ states of Ca^{2+},[43] which is consistent with the core level of CS. The fitted Si 2p spectra are shown in Figure 3, where the peaks at 102.3 eV belong to Si 2p, confirming the presence of Si.[44]

3.1.3. SEM Analysis. The pore structures of diatomaceous earth and eggshell powder are demonstrated in Figure 4a,b,d,e,

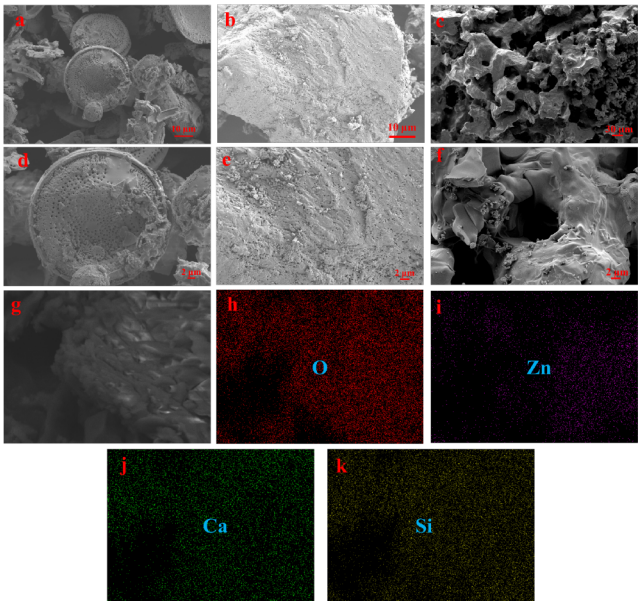

Figure 4. (a, d) Electron microscopy images of diatomaceous earth. (b,e) Electron microscopy images of eggshell powder. (c,f) Electron microscopy images of ZnO−CS. (g−k) Elemental mapping images of ZnO−CS.

respectively. The pore structures of diatomaceous earth and eggshell powder were approximately 200−400 nm in size. The internal structure of ZnO−CS agglomerates was observed by electron microscopy (Figure 4c,f). Pores of different sizes and irregular shapes were found inside, ranging from a few microns to tens of microns. This is likely due to the chemical reaction between diatomaceous earth and eggshell powder during high-

https://doi.org/10.1021/acsomega.4c00904
ACS Omega 2024, 9, 19440−19450

temperature calcination, resulting in the fusion of pores to the micron level. At the macroscopic level, such as in scaffolds, the minimum requirement for pore size is considered to be 100 μm, which is suitable for cell growth and development and can meet the requirements for cell migration and facilitate cell transport. However, at the microscopic level, small pores are conducive to creating hypoxic conditions that can induce osteochondral formation before osteogenesis, thus accelerating osteogenesis, a condition that our scaffolds can meet. To further identify the porous structure of ZnO−CS, an overlay of the O, Zn, Ca, and Si EDX maps is shown in Figure 4h−k. All four elements, O, Zn, Ca, and Si were observed. The colors of the elements Zn, Ca, and Si overlap, proving that ZnO and CS are tightly bound together. The intermediate pore structure is black in the mapping diagram, indicating that no elemental distribution was present on the pore surface. Moreover, the color of element Zn is slightly lighter, indicating a low content, which is consistent with the test data summarized in Table 2.

Table 2. Analysis of the EDX Element Proportion in ZnO−CS Nanocomposites

element	percentage by weight	atomic percent
O	36.37	55.33
Si	23.60	20.56
Ca	38.96	23.71
Zn	1.07	0.40
Total	100	100

3.2. Degradation of Scaffolds and pH Variation within the Microenvironment. When ZnO−CS was initially first submerged in an SBF solution, the exchange of Ca^{2+} and H^+ ions with the solution resulted in a rapid increase in the pH value of the solution (Figure 5a). Furthermore, the presence of unreacted CaO in the ZnO−CS caused a reaction with water, forming $Ca(OH)_2$ as it gradually degraded, which further increased the pH of the SBF solution. On day 7, the increase in pH value gradually slowed down, and a plateau was reached. By day 14, the pH reached 9.41, which is relatively high for the human body. However, due to the fluid regulation mechanism within the body, the solution was discharged in time to maintain a relatively stable pH environment. Figure 5b shows the degradation of ZnO−CS agglomerates in the SBF solution. At the beginning of the ZnO−CS immersion, the ZnO−CS surface undergoes a hydration reaction; the internal porous structure is filled by the adsorption of Ca^{2+} and PO_4^{-} ions from the solution, and the hydroxyapatite layer gradually forms. However, with the extension of the immersion time, the material begins to show significant degradation, and the weight loss gradually increases, reaching 4% by day 14. Overall, the prepared ZnO−CS exhibited a relatively low degradation and slow dissolution rates. However, in the human body, the degradation of ZnO−CS would be faster than that in the *in vitro* simulated environment due to the flow of body fluids, resulting in a higher degradation rate.

3.3. Apatite-Forming Ability of ZnO−CS. To evaluate the *in vitro* bioactivity of ZnO−CS, *in vitro* mineralization experiments were performed on the material for 7 days. Figure 6 shows the SEM images of ZnO−CS immersed in SBF solution on days 1, 3, 5, and 7. Sporadic hydroxyapatite mineralized layers, mostly in the form of small pellets and corals, appeared on the material surface on day 1 of immersion. After 5 days of immersion, the surface of the samples was covered with apatite layers in the form of round spheres, and the deposition of apatite layers was more pronounced. By day 7 of immersion, the field of view was completely filled with spherical HAp. This HAp was formed as a self-agglomerate with a litchi-like, burr-like surface and a diameter of approximately 1 μm. This appearance may be due to the soaking process in which calcium ions were released faster than silica ions, resulting in the formation of a silica-rich layer on the CS surface. Ca^{2+} and PO_4^{3-} ions from the SBF solution then migrate to the composite surface and react with the silica-rich layer to form an amorphous apatite layer. Furthermore, it can be seen in the elemental mapping showed that the content of the P element increased with the number of soaking days, indicating that the formed hydroxyapatite layer became denser over time. Previous studies have demonstrated that this apatite layer is necessary for binding biomaterials to living bone, suggesting that ZnO−CS may have excellent *in vitro* bioactivity and be highly beneficial for bone tissue repair.

3.4. Antibacterial Activity. Recent studies have reported that ZnO possesses excellent antibacterial properties. ZnO can slowly release zinc ions into the medium, which bind to the proteins in bacteria and destroy their protein components, thereby killing the bacteria. Alternatively, ZnO can disrupt the cell membrane of bacteria, leading to the efflux of its contents and rendering the bacteria biologically inactive. As shown in

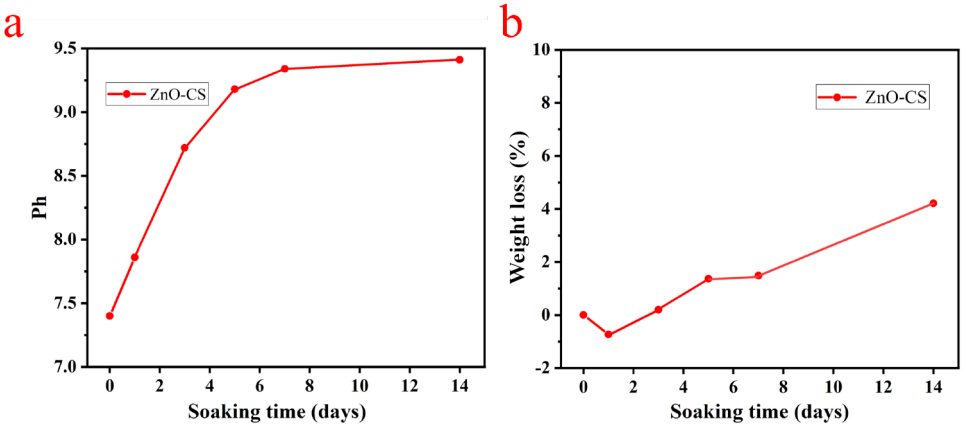

Figure 5. (a) Line graph of the pH change of ZnO−CS agglomerates in the SBF solution. (b) Line graph of the weight variation of ZnO−CS agglomerates in the SBF solution.

https://doi.org/10.1021/acsomega.4c00904
ACS Omega 2024, 9, 19440−19450

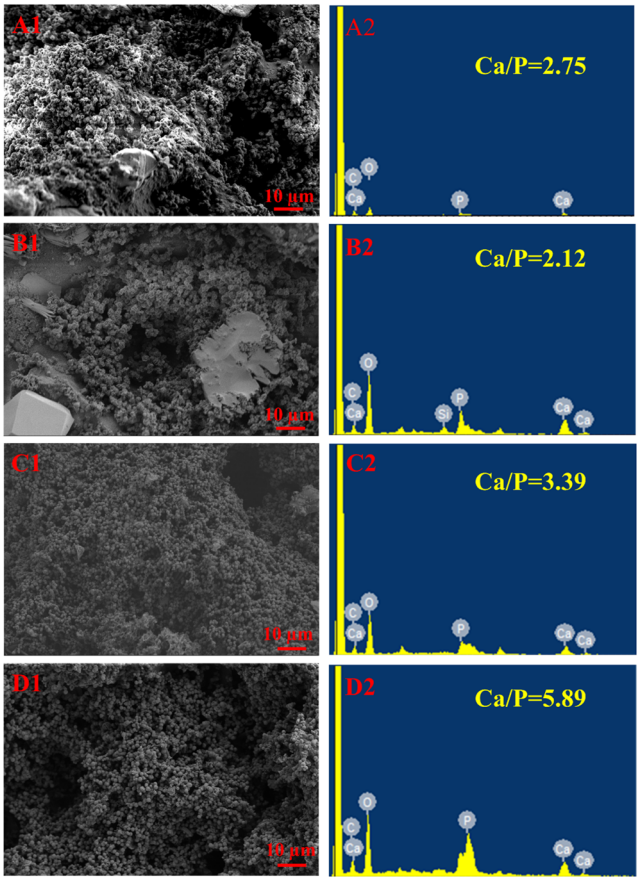

Figure 6. SEM images of wollastonite after degradation studies in SBF. (A1, B1, C1, and D1) Electron microscope images of surface HAp on days 1, 3, 5, and 7, respectively. (A2, B2, C2, and D2) The results of EDX analysis of material surface on days 1, 3, 5, and 7, respectively.

Figure 7, the radius of the inhibition circle for CS without ZnO is only 0.1−0.3 cm, indicating weak inhibition effects. This antibacterial property may be related to the weak alkaline environment caused by the dissolution of CS. In contrast, the radius of the inhibition circle (0.5−0.7 cm) of ZnO−CS for *E. coli* and *S. aureus* was significantly increased. Therefore, the composite material exhibited a significant antibacterial effect on both *E. coli* and *S. aureus*, with greatly improved antibacterial performance. In addition, according to the results of the plate counting method, CS itself had a partial antibacterial effect due to the alkaline environment, but the antibacterial effect was not significant. On the other hand, ZnO−CS reached 98% for *S. aureus* and 99% for *E. coli* due to the presence of ZnO. The experimental results were consistent with the circle of inhibition method. Moreover, as ZnO−CS gradually degrades, ZnO slowly dissolves to release Zn^{2+} ions for a long-term antibacterial effect. This excellent antibacterial property enables the material to inhibit bacterial proliferation when implanted in the human body, thereby facilitating wound repair.

3.5. Evaluation of Cytotoxicity *In Vitro*. To verify the cytotoxicity of the ZnO−CS material, cytotoxicity experiments were performed using MG-63 cells. The experimental results are listed in Figure 8. None of the groups exhibited cytotoxicity under the influence of different concentrations of ZnO−CS (cell viability was not lower than 75% of the control group).[45] The cytotoxicity test revealed that the cell viability of the

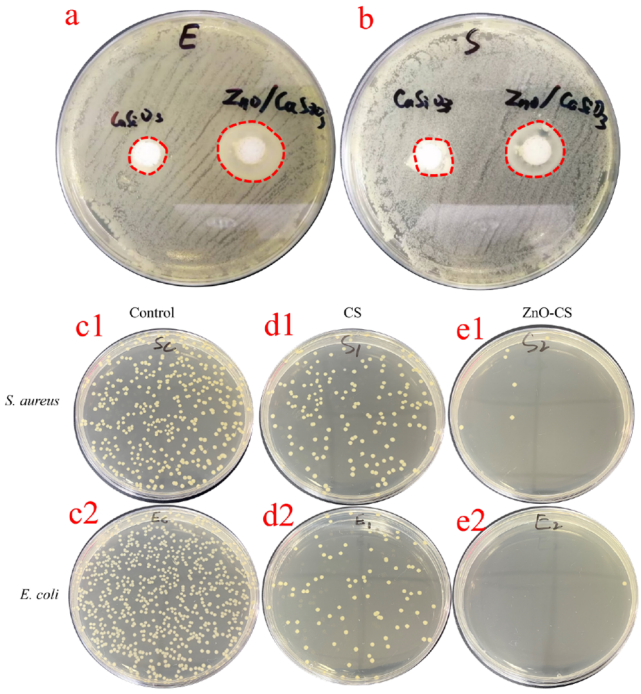

Figure 7. (a) shows the antibacterial effect against *E. coli* , and (b) shows the antibacterial effect against *S. aureus*. (c1), (d1), and (e1) are the bacteriostatic effects of the blank group, CS group, and ZnO−CS group on *S. aureus*, respectively. (c2), (d2), and (e2) are the bacteriostatic effects of the blank group, CS group and ZnO−CS group on *E. col*, respectively.

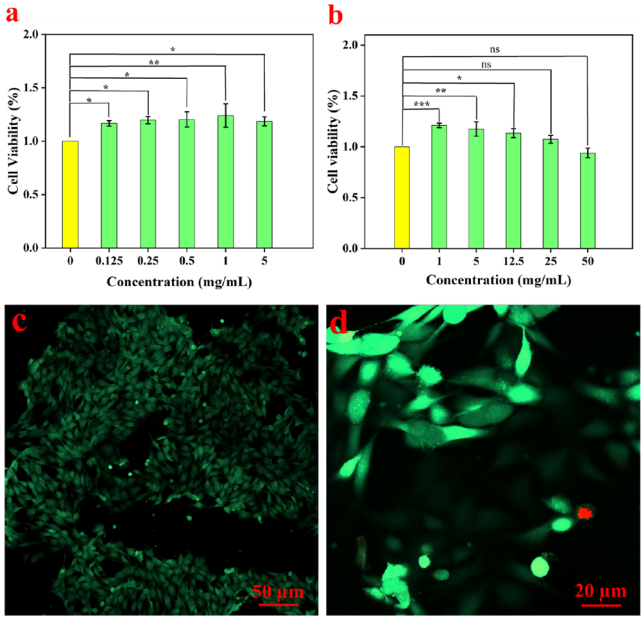

Figure 8. (a) Cell viability (% of control) at ZnO−CS concentrations of 0.125−5 mg/mL. (b) The cell viability (% of control) at ZnO−CS concentrations of 1−50 mg/mL (n = 3, mean ± SD). *p < 0.05, **p < 0.01, and ***p < 0.001. (c,d) Live and dead staining of cells under ZnO−CS.

experimental group was higher than that of the control group when the concentration ranged from 0.125 to 5 mg/mL. This indicated that the ZnO−CS material was not cytotoxic and had a proliferative effect on the cells. With an increase in ZnO−CS concentration, the cell viability initially increased and then

https://doi.org/10.1021/acsomega.4c00904
ACS Omega 2024, 9, 19440−19450

decreased, with the optimal concentration being 1 mg/mL and the cell viability being 124.4% of the control group value. To explore the range of cell biosafety, a second set of experiments was conducted to expand the concentration range of the ZnO−CS material. The results showed that when the concentration was increased to 50 mg/mL, the cell viability did not exhibit cytotoxicity despite a decrease in cell viability. In addition, we performed live−dead cell staining of the cells after the action of ZnO−CS using confocal microscopy, and the results showed that a vast majority of the cells in the Petri dishes were live cells. We selected an area to zoom in to observe the cell morphology and found that the live cells were fibrillar and boat-shaped with full cellular morphology. Dead cells are spherical due to death crumpling, and the nuclei are stained red. This demonstrates that ZnO−CS has excellent biosafety and a wide biosafety range, providing direct evidence to be further investigated via clinical studies.

3.6. Cell Proliferation Assay *In Vitro*. To further assess the material's ability to promote bone regeneration, we selected MG-63 cells to investigate cell proliferation. The results in Figure 9 indicate that ZnO−CS has a significant

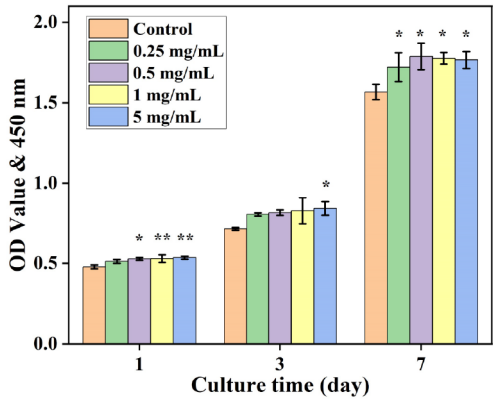

Figure 9. Cell proliferation activity of MG − 63 human osteoblasts cultured in different matrices for 1, 3, and 7 days (n = 3, mean ± SD). *p < 0.05, **p < 0.01.

promotion effect on cell proliferation. The most significant effect was observed on the first day, with a proliferation rate of 112.2%, followed by a stable effect over the subsequent 7 days. The optimal proliferation concentration ranged from 0.5 to 1 mg/mL, which is consistent with the results obtained from the cytotoxicity assay. On day 7, ZnO−CS at a concentration of 0.5 mg/mL had a stronger effect on cell proliferation promotion than the other three groups. As the number of days increased, the promotion effect on cell proliferation became more pronounced at higher concentrations. Moreover, the cell proliferation experiments demonstrated the stable ability of ZnO−CS to promote the cell proliferation.

3.7. *In Vivo* Study. *3.7.1. CT Analysis.* CT scans were used to analyze bone repair in rat cranial defects. The results after 3D reconstruction are shown in Figure 10. In the control group, partial defect repair was observed at 4 weeks with partial bone ingrowth visible at the edges. However, at 8 weeks, there was still no significant bone repair observed in the rats. This demonstrates that 5 mm is the critical threshold for bone repair in rats, but the occurrence of bone ingrowth at the edges at 4 weeks may be due to individual differences or the modeling of rat defects that were less than 5 mm. In the

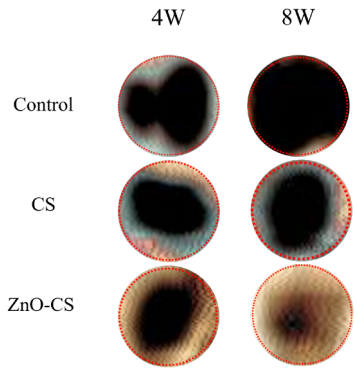

Figure 10. Evaluation of the bone defect repair potential of CS and ZnO−CS *in vivo*. CT imaging analysis of cranial defects in rats 4 and 8 weeks after implantation.

experimental group, significant bone repair was already evident at 4 weeks, although some defects remained unrepaired in the center. By 8 weeks, the defect site showed further repair, with scattered newly formed bone observed within the defect. This confirms the osteogenic effect of the novel CS material. Moreover, the ZnO−CS group exhibited a more pronounced bone defect repair than the CS group, with only a small central defect remaining at 8 weeks. This can be attributed to the action of ZnO, which promotes osteoblast proliferation and bone matrix deposition, thus facilitating bone defect repair. Furthermore, due to its antibacterial properties, ZnO can kill bacteria at the site of bone defects, preventing infection and leading to more significant repair in the ZnO−CS group. The same conclusion was reached by Babu et al.[46] who doped bioactive phosphate glasses with ZnO. It was demonstrated that the doping of ZnO significantly increased the cell viability and proliferation rate after 3 days of culture.

It should be noted that CT imaging results may not fully capture the internal formation of new bone compared to images produced by micro-CT. Insufficient bone density in some of the new bone formations led to an inadequate visualization of the central defect in the CS group. However, the current results still demonstrate the excellent osteogenic effect of CS. This underscores the potential application of novel calcium silicate materials in the field of bone tissue engineering.

3.7.2. Histological Analysis. The process of bone repair is a rather lengthy process involving various growth factors and various cellular regulatory processes.[47] H and E staining and Masson special staining were used for staining analysis of the new bone tissue, and the results are shown in Figure 11. At 4 weeks, fibrous connective tissue was generated in the defects of the blank group, and the formation of new bone tissue was largely absent. By 8 weeks, there was fibrous connective tissue generation and some new bone tissue formation within the defects. In the CS group, at 4 weeks, the defect was filled with implant material wrapped by fibrous connective tissue. The implant material was not completely degraded, and phagocytes and multinucleated giant cells were observed within the implant material. Neoblasts and some blood vessels were observed within the defect at 8 weeks. In the ZnO−CS group, due to the incorporation of ZnO material, the repair effect was better. By 8 weeks, many of phagocytes and multinucleated giant cells could be seen in the implanted material, and neoplastic bone formation and angiogenesis was observed within the defects. Compared to that of the blank group, the

https://doi.org/10.1021/acsomega.4c00904
ACS Omega 2024, 9, 19440−19450

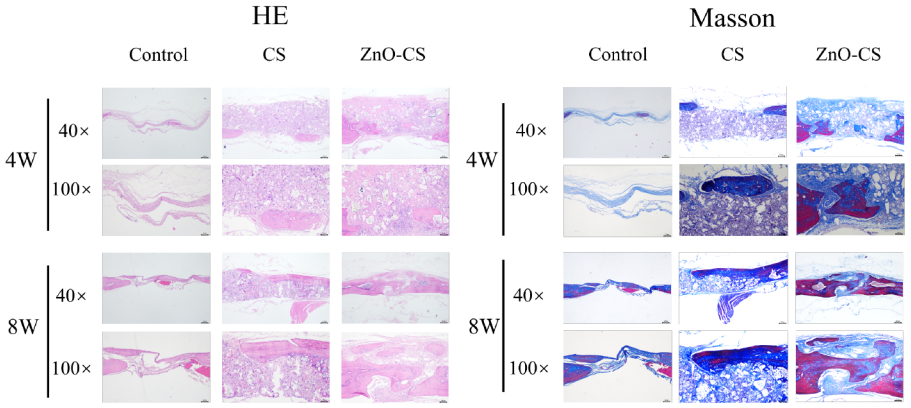

Figure 11. Hematoxylin and eosin (H and E) and Masson staining results of CS and ZnO−CS materials at 4 and 8 weeks.

bone repair effect within the ZnO−CS group was gradually enhanced. The ZnO−CS group showed the best performance in new bone tissue formation and angiogenesis.

In the Masson staining images, the muscle fibers and collagen fiber connective tissue were stained red and blue, respectively. After 8 weeks of the experiment, only a small amount of neoplastic bone tissue was observed in the blank group, while the CS−ZnO-treated group exhibited more pronounced immature bone tissue, confirming the superior repair ability of the ZnO−CS material. At 8 weeks post implantation, a small amount of mature bone tissue was observed in the CS-treated group, indicating that the ZnO−CS material had a higher inherent bone healing ability than CS alone. Notably, significantly more mature bone tissue was observed in the defect area treated with the ZnO−CS material, demonstrating the most substantial bone regeneration. Both H and E and Masson staining consistently highlighted the optimal osteogenic activity of the ZnO−CS material, which significantly promoted bone tissue regeneration.

4. CONCLUSIONS

In this study, we successfully prepared ZnO−CS nanocomposites via high-temperature calcination using eggshells and diatomaceous earth as the raw material. Through electron microscopy, we observed that the nanocomposites retained the porous structure of their precursors. The prepared nanocomposites were characterized and tested for their degradability, *in vitro* mineralization ability, and antibacterial properties. Our test results showed that the ZnO−CS material was highly biocompatible, exhibited some degradability, and generated a relatively alkaline environment, which inhibited bacterial proliferation. The inclusion of ZnO in the material specifically led to strong inhibition of two common pathogenic bacteria (*E. coli* and *S. aureus*). These characteristics suggest that ZnO−CS nanocomposites have great potential as novel bone graft material. Future clinical studies are required to validate these findings.

AUTHOR INFORMATION

Corresponding Author

Wenhua Wu − *Department of Spinal Surgery, The Second Clinical Medical College of Fujian Medical University, The Second Affiliated Hospital of Fujian Medical University, Quanzhou, Fujian 362000, China*; Email: drwuwenhua@126.com

Authors

Haiming Yu − *Department of Spinal Surgery, The Second Clinical Medical College of Fujian Medical University, The Second Affiliated Hospital of Fujian Medical University, Quanzhou, Fujian 362000, China*; orcid.org/0000-0002-9280-2371

Zhihua Liu − *Department of Spinal Surgery, The Second Clinical Medical College of Fujian Medical University, The Second Affiliated Hospital of Fujian Medical University, Quanzhou, Fujian 362000, China*

Lingying Chen − *Department of Spinal Surgery, The Second Clinical Medical College of Fujian Medical University, The Second Affiliated Hospital of Fujian Medical University, Quanzhou, Fujian 362000, China*

Xiaoyu He − *Department of Spinal Surgery, The Second Clinical Medical College of Fujian Medical University, The Second Affiliated Hospital of Fujian Medical University, Quanzhou, Fujian 362000, China*

Yiyong Weng − *Department of Spinal Surgery, The Second Clinical Medical College of Fujian Medical University, The Second Affiliated Hospital of Fujian Medical University, Quanzhou, Fujian 362000, China*

Weizhe Li − *Department of Spinal Surgery, The Second Clinical Medical College of Fujian Medical University, The Second Affiliated Hospital of Fujian Medical University, Quanzhou, Fujian 362000, China*

Xiaozhi Zheng − *Department of Spinal Surgery, The Second Clinical Medical College of Fujian Medical University, The Second Affiliated Hospital of Fujian Medical University, Quanzhou, Fujian 362000, China*; orcid.org/0009-0004-4189-0043

Qunlong Pan − *Department of Spinal Surgery, The Second Clinical Medical College of Fujian Medical University, The Second Affiliated Hospital of Fujian Medical University, Quanzhou, Fujian 362000, China*

Rongmou Zhang − *Department of Spinal Surgery, The Second Clinical Medical College of Fujian Medical University, The Second Affiliated Hospital of Fujian Medical University, Quanzhou, Fujian 362000, China*

Xiaoyan Zhang − *Key Laboratory of Chemical Materials and Green Nanotechnology, College of Chemical Engineering and Materials Science, Quanzhou Normal University, Quanzhou, Fujian 362000, China*; orcid.org/0000-0002-5816-8178

Complete contact information is available at: https://pubs.acs.org/10.1021/acsomega.4c00904

https://doi.org/10.1021/acsomega.4c00904
ACS Omega 2024, 9, 19440−19450

Author Contributions

[§]H.Y. and Z.L. have contributed equally to this work.

Notes

The authors declare no competing financial interest.

■ ACKNOWLEDGMENTS

This work was financially supported by the Quanzhou Science and Technology Bureau (project number 2021C057R), Fuxiaquan Collaborative Innovation Platform (K30001), and Fujian Provincial Key Science and Technology Project (2022G02029). The study was supported by the Research Fund for PhD Tutorship of the Second Affiliated Hospital of Fujian Medical University (No. 2022BD1702).

■ REFERENCES

(1) Oryan, A.; Alidadi, S. Reconstruction of radial bone defect in rat by calcium silicate biomaterials. *Life Sci.* **2018**, *201*, 45−53.
(2) Namdar, A.; Salahinejad, E. Advances in ion-doping of Ca-Mg silicate bioceramics for bone tissue engineering. *Coord. Chem. Rev.* **2023**, *478*, 215001.
(3) Sha, S.; Qiu, F.; Li, S.; Liu, J.; Xu, H.; Tang, J.; Zhang, Y. A modified calcium silicate composite bone cement prepared from polyethylene glycol and graphene oxide for biomaterials. *Mater. Today Commun.* **2021**, *27*, 102431.
(4) Fu, Z.; Li, D.; Cui, J.; Xu, H.; Yuan, C.; Wang, P.; Zhao, B.; Lin, K. Promoting bone regeneration via bioactive calcium silicate nanowires reinforced poly (ε-caprolactone) electrospun fibrous membranes. *Mater. Design* **2023**, *226*, 111671.
(5) Chen, C. Y.; Shie, M. Y.; Lee, A. K.; Chou, Y. T.; Chiang, C.; Lin, C. P. 3D-Printed Ginsenoside Rb1-Loaded Mesoporous Calcium Silicate/Calcium Sulfate Scaffolds for Inflammation Inhibition and Bone Regeneration. *Biomedicines* **2021**, *9* (8), 907.
(6) Conway, J. C.; Oliver, R. A.; Wang, T.; Wills, D. J.; Herbert, J.; Buckland, T.; Walsh, W. R.; Gibson, I. R. The efficacy of a nanosynthetic bone graft substitute as a bone graft extender in rabbit posterolateral fusion. *Spine J.* **2021**, *21* (11), 1925−1937.
(7) Wang, P.; Gong, Y.; Zhou, G.; Ren, W.; Wang, X. Biodegradable Implants for Internal Fixation of Fractures and Accelerated Bone Regeneration. *ACS Omega* **2023**, *8* (31), 27920−27931.
(8) Wanasingha, N.; Dutta, N. K.; Choudhury, N. R. Emerging bioadhesives: from traditional bioactive and bioinert to a new biomimetic protein-based approach. *Adv. Colloid Interface Sci.* **2021**, *296*, 102521.
(9) Pal, A.; Das Karmakar, P.; Vel, R.; Bodhak, S. Synthesis and Characterizations of Bioactive Glass Nanoparticle-Incorporated Triblock Copolymeric Injectable Hydrogel for Bone Tissue Engineering. *ACS Appl. Bio Mater.* **2023**, *6* (2), 445−457.
(10) Fu, Z.; Ouyang, L.; Xu, R.; Yang, Y.; Sun, W. Responsive biomaterials for 3D bioprinting: A review. *Mater. Today* **2022**, *52*, 112−132.
(11) Yan, M.; Zhao, Y.; Dai, Y.; Yao, X.; Dai, H. Modified calcium magnesium phosphate bone cement with improved microenvironment. *Ceram. Int.* **2022**, *48* (22), 32929−32936.
(12) Yao, S.; Xie, Z.-A.; Ye, L.; Jin, B.; Xu, Y.; Wang, M.; Yu, C.; Tang, R.; Fang, X.; Fan, S. Ultrasmall sized calcium phosphate nanoclusters based organic-inorganic biofiber for accelerated bone fracture healing. *Mater. Today Nano* **2023**, *21*, 100290.
(13) Ho, C.-C.; Wei, C.-K.; Lin, S.-Y.; Ding, S.-J. Calcium silicate cements prepared by hydrothermal synthesis for bone repair. *Ceram. Int.* **2016**, *42* (7), 9183−9189.
(14) Fiocco, L.; Li, S.; Stevens, M. M.; Bernardo, E.; Jones, J. R. Biocompatibility and bioactivity of porous polymer-derived Ca-Mg silicate ceramics. *Acta Biomater.* **2017**, *50*, 56−67.
(15) Pan, Y.; Yin, J.; Zuo, K.; Yao, D.; Xia, Y.; Liang, H.; Zeng, Y. The sintering behavior and mechanical properties of CaSiO3 bioceramics with B2O3 addition. *Ceram. Int.* **2016**, *42* (7), 9222−9226.
(16) Kee, C. C.; Ang, B. C.; Metselaar, H. S. C. Synthesis of europium-doped calcium silicate hydrate via hydrothermal and coprecipitation method. *Ceram. Int.* **2021**, *47* (4), 4803−4812.
(17) Zakira, U.; Bajpayee, A.; Pharr, M.; Banerjee, S.; Birgisson, B. Grid nanoindentation on calcium sulfoaluminate (CSA)-Kaolinite pastes. *Constr. Build. Mater.* **2022**, *335*, 127523.
(18) Paruthi, S.; Khan, A. H.; Kumar, A.; Kumar, F.; Hasan, M. A.; Magbool, H. M.; Manzar, M. S. Sustainable cement replacement using waste eggshells: A review on mechanical properties of eggshell concrete and strength prediction using artificial neural network. *Case Stud. Constr. Mater.* **2023**, *18*, No. e02160.
(19) Zhang, X.; He, X.; Kang, Z.; Cui, M.; Yang, D.-P.; Luque, R. Waste Eggshell-Derived Dual-Functional CuO/ZnO/Eggshell Nanocomposites: (Photo)catalytic Reduction and Bacterial Inactivation. *ACS Sustainable Chem. Eng.* **2019**, *7* (18), 15762−15771.
(20) Yang, D.-P.; Li, Z.; Liu, M.; Zhang, X.; Chen, Y.; Xue, H.; Ye, E.; Luque, R. Biomass-Derived Carbonaceous Materials: Recent Progress in Synthetic Approaches, Advantages, and Applications. *ACS Sustainable Chem. Eng.* **2019**, *7* (5), 4564−4585.
(21) Chu, Z.; Wang, Z.; Chen, L.; Wang, X.; Huang, C.; Cui, M.; Yang, D.-P.; Jia, N. Combining Magnetic Resonance Imaging with Photothermal Therapy of CuS@BSA Nanoparticles for Cancer Theranostics. *ACS Appl. Nano Mater.* **2018**, *1* (5), 2332−2340.
(22) Zhang, Y.; Xue, C.; Zhang, Y.; Zhang, Q.; Zhang, K.; Liu, Y.; Shan, Z.; Qiu, W.; Chen, G.; Li, N. Cocktail effect of ionic patch driven by triboelectric nanogenerator for diabetic wound healing. *Chin. Chem. Lett.* **2023**, No. 109196.
(23) Guo, Y.; Sun, Y.; Yang, D.-P.; Dai, J.; Liu, Z.; Chen, Y.; Huang, J.; Li, Q. Biogenic Pt/CaCO3 Nanocomposite as a Robust Catalyst toward Benzene Oxidation. *ACS Appl. Mater. Interfaces* **2020**, *12* (2), 2469−2480.
(24) Liu, W.; Tang, C.; Cai, Z.; Jin, Y.; Ahn, D. U.; Huang, X. The effectiveness of polypeptides from phosvitin and eggshell membrane in enhancing the bioavailability of eggshell powder calcium and its accumulation in bones. *Food Biosci.* **2023**, *51*, 102257.
(25) Zhang, X.; Zhou, J.; Yang, D.-P.; Chen, S.; Huang, J.; Li, Z. Cu2-xS loaded diatom nanocomposites as novel photocatalysts for efficient photocatalytic degradation of organic pollutants. *Catal. Today* **2019**, *335*, 228−235.
(26) Li, L.; Liu, X.; He, S.; Cao, H.; Su, B.; Huang, T.; Chen, Q.; Liu, M.; Yang, D.-P. Electrochemiluminescence Immunosensor Based on Nanobody and Au/CaCO3 Synthesized Using Waste Eggshells for Ultrasensitive Detection of Ochratoxin A. *ACS Omega* **2021**, *6* (44), 30148−30156.
(27) Wu, S.-C.; Hsu, H.-C.; Yu, H.-C.; Shen, C.-E.; Ho, W.-F. Preparation and evaluation of osteoinductive porous biphasic calcium phosphate granules obtained from eggshell for bone tissue engineering. *Adv. Powder Technol.* **2023**, *34* (1), 103909.
(28) Janini, A. C. P.; Bombarda, G. F.; Pelepenko, L. E.; Marciano, M. A. Antimicrobial Activity of Calcium Silicate-Based Dental Materials: A Literature Review. *Antibiotics (Basel, Switz.)* **2021**, *10* (7), 865.
(29) Leng, D.; Li, Y.; Zhu, J.; Liang, R.; Zhang, C.; Zhou, Y.; Li, M.; Wang, Y.; Rong, D.; Wu, D. The Antibiofilm Activity and Mechanism of Nanosilver- and Nanozinc-Incorporated Mesoporous Calcium-Silicate Nanoparticles. *Int. J. Nanomed.* **2020**, *15*, 3921−3936.
(30) Lu, J.; Zhou, B.; Zhang, X.; Zhao, X.; Liu, X.; Wu, S.; Yang, D.-P. Oyster shell-derived CuFe2O4-Hap nanocomposite for healthy houses: Bacterial and formaldehyde elimination. *Chem. Eng. J.* **2023**, *477*, 147054.
(31) Ramani, M.; Ponnusamy, S.; Muthamizhchelvan, C.; Cullen, J.; Krishnamurthy, S.; Marsili, E. Morphology-directed synthesis of ZnO nanostructures and their antibacterial activity. *Colloids Surf., B* **2013**, *105*, 24−30.
(32) Tang, Y. A.; Sun, H.; Qin, Z.; Yin, S. Y.; Tian, L. M.; Liu, Z. N. Bioinspired photocatalytic ZnO/Au nanopillar-modified surface for enhanced antibacterial and antiadhesive property. *Chem. Eng. J.* **2020**, *398*, 125575.

https://doi.org/10.1021/acsomega.4c00904
ACS Omega 2024, 9, 19440−19450

(33) Chang, L.; Feng, Y.; Wang, B.; Huang, X.; Yang, D.-P.; Lu, Y. Dual functional oyster shell-derived Ag/ZnO/CaCO3 nanocomposites with enhanced catalytic and antibacterial activities for water purification. *RSC Adv.* **2019**, *9* (70), 41336−41344.
(34) Hwangbo, M.; Claycomb, E. C.; Liu, Y. N.; Alivio, T. E. G.; Banerjee, S.; Chu, K. H. Effectiveness of zinc oxide-assisted photocatalysis for concerned constituents in reclaimed wastewater: 1,4-Dioxane, trihalomethanes, antibiotics, antibiotic resistant bacteria (ARB), and antibiotic resistance genes (ARGs) (vol 649, pg 1189, 2019). *Sci. Total Environ.* **2019**, *655* (655), 1515−1515.
(35) Felice, B.; Sánchez, M. A.; Socci, M. C.; Sappia, L. D.; Gómez, M. I.; Cruz, M. K.; Felice, C. J.; Martí, M.; Pividori, M. I.; Simonelli, G.; et al. Controlled degradability of PCL-ZnO nanofibrous scaffolds for bone tissue engineering and their antibacterial activity. *Mater. Sci. Eng.* **2018**, *93*, 724−738.
(36) Kokubo, T.; Takadama, H. How useful is SBF in predicting in vivo bone bioactivity? *Biomaterials* **2006**, *27* (15), 2907−2915.
(37) Spicer, P. P.; Kretlow, J. D.; Young, S.; Jansen, J. A.; Kasper, F. K.; Mikos, A. G. Evaluation of bone regeneration using the rat critical size calvarial defect. *Nat. Protoc.* **2012**, *7* (10), 1918−1929.
(38) Zheng, Q.; Jiang, J.; Li, X.; Bustillo, K. C.; Zheng, H. In situ TEM observation of calcium silicate hydrate nanostructure at high temperatures. *Cem. Concr. Res.* **2021**, *149*, 106579.
(39) Mabrouk, M.; Mousa, S. M.; Shalaby, M. B.; Shalby, A. B.; Beherei, H. H.; Das, D. B. Egyptian corals-based calcium silicate (CaS) nanopowders doped with zinc/copper for improved chemical stability and treatment of calvarial defects. *Colloids Surf., A* **2023**, *660*, 130875.
(40) Mabrouk, M.; Beherei, H. H.; Tanaka, Y.; Tanaka, M. Sol-gel silicate glass doped with silver for bone regeneration: Antibacterial activity, intermediate water, and cell death mode. *Biomater. Adv.* **2022**, *138*, 212965.
(41) Li, Z.; Yang, D.-P.; Chen, Y.; Du, Z.; Guo, Y.; Huang, J.; Li, Q. Waste eggshells to valuable Co3O4/CaCO3 materials as efficient catalysts for VOCs oxidation. *Mol. Catal.* **2020**, *483*, 110766.
(42) Sasireka, A.; Suganthi, S.; Vignesh, S.; Raj, V.; Oh, T. H. Preparation and characterization of zinc modified calcium silicate/polycaprolactone with graphene oxide composite coating for bone repair applications. *Ceram. Int.* **2023**, *49* (12), 20251−20260.
(43) Cheng, M.; Zeng, G.; Huang, D.; Lai, C.; Liu, Y.; Xu, P.; Zhang, C.; Wan, J.; Hu, L.; Xiong, W.; et al. Salicylic acid−methanol modified steel converter slag as heterogeneous Fenton-like catalyst for enhanced degradation of alachlor. *Chem. Eng. J.* **2017**, *327*, 686−693.
(44) Huang, Q.; Liu, X.; Elkhooly, T. A.; Zhang, R.; Shen, Z.; Feng, Q. A novel titania/calcium silicate hydrate hierarchical coating on titanium. *Colloids Surf., B* **2015**, *134*, 169−177.
(45) Mansoori-Kermani, A.; Mashayekhan, S.; Kermani, F.; Abdekhodaie, M. J. The effect of tricalcium silicate incorporation on bioactivity, injectability, and mechanical properties of calcium sulfate/bioactive glass bone cement. *Ceram. Int.* **2023**, *49* (10), 15003−15014.
(46) Babu, M. M.; Rao, P. V.; Singh, R. K.; Kim, H.-W.; Veeraiah, N.; Özcan, M.; Prasad, P. S. ZnO incorporated high phosphate bioactive glasses for guided bone regeneration implants: enhancement of in vitro bioactivity and antibacterial activity. *J. Mater. Res. Technol.* **2021**, *15*, 633−646.
(47) He, H.; Wang, L.; Cai, X.; Wang, Q.; Liu, P.; Xiao, J. Biomimetic collagen composite matrix-hydroxyapatite scaffold induce bone regeneration in critical size cranial defects. *Mater. Design* **2023**, *236*, 112510.

https://doi.org/10.1021/acsomega.4c00904
ACS Omega 2024, 9, 19440−19450